ChemComm

Synergistic photothermal and photochemical partial oxidation of methane over noble metals incorporated in mesoporous silica

Journal:	*ChemComm*
Manuscript ID	CC-COM-08-2019-006170.R1
Article Type:	Communication

COMMUNICATION

Synergistic photothermal and photochemical partial oxidation of methane over noble metals incorporated in mesoporous silica

Received 00th January 20xx,
Accepted 00th January 20xx

DOI: 10.1039/x0xx00000x

Haoyang Jiang, [a] Xiaobo Peng, [b] Akira Yamaguchi,[a] Takeshi Fujita,[c] Hideki Abe,[b] and Masahiro Miyauchi *[a]

A hot-carrier-driven photocatalytic system was established by incorporating noble metals (Rh, Pd, Ru, and Pt) in a mesoporous silica (MCM-41) for the partial oxidation of methane (POM) under ultraviolet (UV) irradiation. The Rh/MCM photocatalyst initiated POM at a mild operating temperature of 423 K with syngas generation. The reaction was identified as a synergistic photothermal and photochemical process.

The conversion of methane to high-value-added fuel or chemical products is a prospective approach that can realize the integrated utilization of natural gas resources. Among various methane conversion reactions, the partial oxidation of methane with O_2 (POM, $CH_4 + ½\ O_2 \rightarrow CO + 2\ H_2$) is a cost-efficient and easy-to-build catalytic reaction to produce syngas including carbon monoxide and hydrogen. These are essential raw materials for producing valuable organic compounds like methanol and liquid hydrocarbons through hydrogenation or the Fischer–Tropsch process.[1] However, the critical scientific problem is that conventional thermocatalytic POM is difficult to proceed under moderate conditions owing to the following reasons. First, CH_4 molecules are extremely stable and difficult to be activated. Second, POM is mildly exothermic, while complete oxidation to CO_2 and H_2O, which is a strongly exothermic reaction, is more favourable at low temperatures.[2] It is urgent to solve this scientific problem in order to accelerate the progress of C1 chemistry and facilitate the popularization of methane conversion technology.

Photocatalysis is considered a crucial tool that enables chemical reactions to proceed under moderate temperature conditions by converting photon energy to chemical energy.[3] For example, photocatalytic methane dry reforming (DRM) and steam reforming (STM) were reported previously, in which the bandgap excitation in semiconductors drove these reactions.[4] In addition to semiconductor-based photocatalysis, hot-carrier-mediated photocatalysis, usually proceeding on supported metal nanoparticles under illumination, can be induced by the Landau damping of surface plasmon resonance (SPR) in plasmonic metals, such as Au, Ag, and Cu,[5] or direct interband electron transitions in other noble metals including Ru, Rh, Pd, and Pt.[6] Due to the limited lifetime, hot carriers can undergo a rapid nonradiative relaxation process, resulting in the local heating on catalyst surface, known as hot carriers' photothermal effect. On the other hand, part of the highly energized hot carriers can be captured by surface-adsorbed molecules, and stimulate photochemical processes, known as hot carriers' nonthermal effect.

The use of hot carriers has been validated in some gas-phase photocatalytic reactions like CO_2 reduction with H_2 on Rh/Al_2O_3[7] and Al/Cu_2O[8], ethylene and CO oxidation on Ag/Al_2O_3,[9] dye degradation on Pd/Cu_2O,[10] and ammonia decomposition on Cu-Ru.[11] The enhancement of STM or DRM under visible light has been confirmed when using Rh/TiO_2,[12] plasmonic Ni/Al_2O_3,[13] and silica-nanocluster-modified Ni/SiO_2.[14] However, it is still controversial as to whether these reactions proceed via a photothermal or photochemical process. It is expected that the concept of hot-carrier-driven catalysis can also be applied to POM. As noble metals, Ru, Rh, Pd, and Pt are precisely well-known thermocatalysts for methane conversion reactions.[15] Simultaneously, they have significant optical response properties and exhibit strong interband excitation in the ultraviolet (UV) range.[6b,16] Therefore, they are qualified candidates to be used as photocatalysts for POM under moderate temperature conditions. Herein, we focus on mesoporous silica, MCM-41, as the support of metals. The mesopores in MCM-41 enable uniform immobilization of metal nanoparticles. Additionally, silica is an optically inert material that does not interrupt the absorption properties of metals or the optical response process. We investigated the photocatalytic properties of noble metals incorporated in

[a] *Department of Materials Science and Engineering, Tokyo Institute of Technology, 2-12-1 Ookayama, Meguro, Tokyo 152-8552, Japan. E-mail: miyauchi@ceram.titech.ac.jp*
[b] *National Institute for Materials Science (NIMS), 1-1 Namiki, Tsukuba, Ibaraki 305-0044, Japan.*
[c] *School of Environmental Science and Engineering, Kochi University of Technology, 185 Miyanokuchi, Tosayamada, Kami, Kochi 782-8502, Japan.*
Electronic Supplementary Information (ESI) available. See DOI: 10.1039/x0xx00000x

MCM-41 in the POM reaction under UV illumination, at different operation temperatures, and identified the photocatalytic mechanism involving the generation, relaxation, and transportation of hot carriers. We demonstrated the importance of metal components in the photocatalytic POM and discovered that Rh exhibits superb low-temperature activity for syngas generation. We carefully examined the contribution of photothermal and/or photochemical nonthermal effects to the POM activity under UV irradiation in the present system.

MCM-41 incorporated with noble metals, denoted M/MCMs (M = Ru, Rh, Pd, or Pt), were synthesized by one-pot precipitation followed by calcination and reduction treatment (Note 1, ESI†). The wide-angle X-ray diffraction (XRD) patterns are shown in Fig. 1. The broad diffraction peak around 2ϑ = 22.5°, observed for all the samples, is assigned to amorphous silica, which forms the backbone of MCM-41. Ru/MCM and Pt/MCM show sharp and intense peaks that are attributed to the phases of metallic Ru and Pt, respectively. In contrast, the peaks of metallic phases in Rh and Pd/MCMs were weak and broad, although the feed molar ratios of metal/silica were identical for all the samples. These results imply that the grain sizes of Rh and Pd particles were much smaller than those of Ru and Pt. The small-angle X-ray scattering (SAXS) patterns (Fig. 1b) of M/MCMs exhibited an evident peak of the plane (100), demonstrating the formation of a mesoporous structure. The corresponding d_{100} spacings calculated from the q values were in the range 3.6–3.9 nm and were close to d_{100} of the commercial MCM-41 (3.6 nm) purchased from Sigma Aldrich.

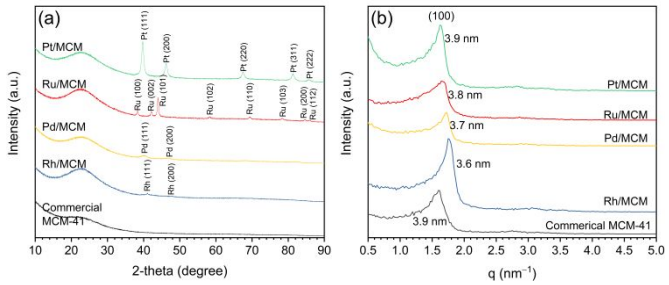

Fig. 1 (a) XRD and (b) SAXS patterns of commercial MCM-41 and synthesized MCM-41 incorporated with Ru, Rh, Pd, and Pt.

The transmission electron microscope (TEM) images of the synthesized samples and the statistical estimation of the metal particle size distribution are shown in Fig. S1 (ESI†). In Rh/MCM and Pd/MCM, small metal nanoparticles with sizes of 3.2 and 3.5 nm were homogeneously dispersed in MCM-41. In Ru/MCM, a large metal particle with a size over 30 nm was located at the boundaries of agminated MCM-41 particles, and we did not observe any metallic Ru species in the porous structure of MCM-41. In Pt/MCM, most of the Pt nanoparticles with a mean size of 5.4 nm were observed in the framework of MCM-41 but lacked a uniform dispersion as compared to Rh and Pd/MCMs. The scanning transmission electron microscope (STEM) images of Rh and Pd/MCMs, as shown in Fig. S2 (ESI†), were captured along the [110] direction of MCM-41. The alternately dark and bright stripes indicate the stretch direction of the pore channels. The STEM observation implies that Rh and Pd nanoparticles are finely embedded in these channels.

The UV-vis spectra are displayed in Fig. S3 (ESI†). The absorbance of pristine MCM-41 was almost zero over the UV and visible light range owing to its ultrawide gap property. On the other hand, the absorption of both the visible and UV range in M/MCMs can be assigned to the *d*-to-*s* interband excitation of electrons in metal particles. For Rh, Pd, and Pt/MCMs, the absorption in the UV region was much stronger, suggesting that these nanoparticles would be efficient UV light-harvesting materials. Since the metal loading amounts were the same and the particle sizes of Rh and Pd were similar, the difference in absorbance was mainly determined by the intrinsic optical property of the different metal compositions.

We evaluated the thermocatalytic and photocatalytic activities of M/MCM catalysts using a customized reactor under a flow of Ar-based mixed gas containing 1% CH_4 and 0.5% O_2 (Note 3, ESI†). Fig. 2 shows the yields of CO and CO_2 over M/MCMs under dark and UV irradiation conditions at different operating temperatures below 723 K. The detailed plots involving the temperature dependences of conversions and yields are given in Fig. S4 (ESI†). Under the dark conditions, the transformation of CH_4 over these metals below 523 K was negligible, as only trace amounts of complete oxidation products (CO_2 and H_2O) were detected. The initiation temperatures of POM over Rh, Pd, Ru, and Pt/MCMs were as high as 723, 723, 923, and 823 K, respectively. We observed the effect of UV irradiation on the catalytic activities for all M/MCMs. Evidently, Rh/MCM exhibited superb photocatalytic activity in which POM had already become the dominant reaction at 423 K. The yields of CO and H_2 reached 27% and 44%, respectively, and greatly exceeded the yields of CO_2 (22%) and H_2O (8%). The unbalanced yields of CO and H_2 were attributed to the water-gas shift (WGS, $CO + H_2O \rightarrow CO_2 + H_2$) side reaction. The largest gap in the yields of syngas with and without illumination was observed at 673 K; however, the gap became smaller with a further increase in temperature, indicating that the photocatalytic effect gradually became minor where thermocatalysis played a dominant role at high temperatures. Pd/MCM also performed well under UV irradiation, while syngas generation started at 523 K, at which the yields of CO and H_2 were 41% and 30%, respectively. The higher yield of CO indicates the existence of the reverse water-gas shift (rWGS, $CO_2 + H_2 \rightarrow CO + H_2O$) as a side reaction. However, the yield of H_2 significantly increased to 51%, which exceeded that of CO (43%) at temperatures above 623 K, because the WGS became the primary side reaction. The light effect could not be seen at 1023 K, as the activities with and without illumination were almost the same. Besides, the 20-h durability of Rh and Pd/MCMs was tested at 423 and 523 K, respectively. Rh/MCM exhibited remarkable photocatalytic stability in which the turnover frequency (TOF) for CH_4 stayed in the range 0.101–0.103 s^{-1} (described in detail in Fig. S5, ESI†).

By contrast, Ru and Pt/MCMs showed insufficient photocatalytic activity. To initiate POM, a temperature of 573 K was necessary for Ru/MCM under UV irradiation (Fig. S4f, ESI†). In addition, the thermostability of Ru/MCM was poor, as a

deactivation phenomenon was observed at 1023 K. The photocatalytic effect on Pt/MCM was limited to the complete oxidation of methane at mild temperatures, and there was no change in the initiation temperature of syngas compared with the dark conditions (Fig. S4h, ESI†) even though the optical absorption of Pt/MCM was strong among the present catalysts. Different metals have different electronic structures, which determine their different CH_4 activation ability. According to a theoretical study based on DFT calculation, Rh has the lowest CH_4 dissociation energy for the generation of C* and H* monoatomic intermediate among all the metals, which would be the reason for the outstanding photocatalytic activity.[17]

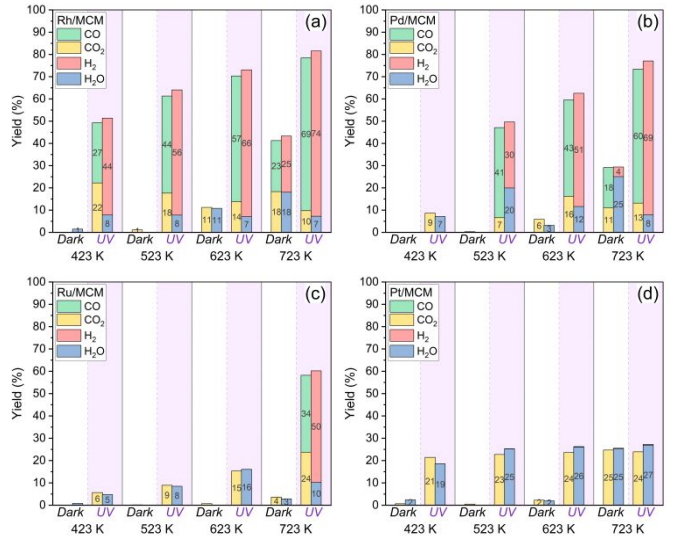

Fig. 2 Catalytic activities for POM over (a) Ru/MCM, (b) Rh/MCM, (c) Pd/MCM, and (d) Pt/MCM under the dark and UV irradiation conditions at different operating temperatures.

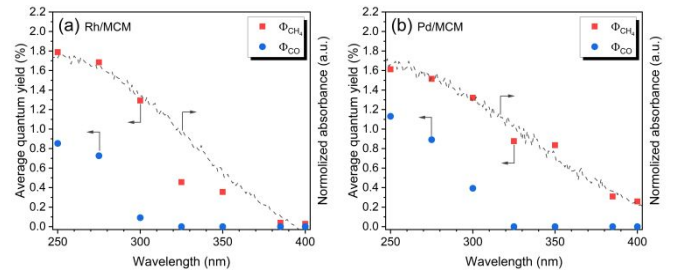

Fig. 3 Action spectra of (a) Rh/MCM at 423 K and (b)Pd/MCM at 523 K in the wavelength range from 250–400 nm.

The photocatalytic mechanism of POM was investigated by plotting the action spectra of Rh and Pd/MCMs, as shown in Fig. 3. A series of long-wave pass filters were used to adjust the wavelength ranges of incident UV light. The calculation of the wavelength-dependent average quantum yields of CH_4 ($\Phi_{CH}4$) and CO (Φ_{CO}) is explained in Note 4 (ESI†). For both catalysts, the variation tendency of $\Phi_{CH}4$ with cutoff wavelengths from 200–400 nm, is broadly consistent with the absorption spectra. This proves that CH_4 conversion was induced by the hot carriers derived from the interband excitation in metals. $\Phi_{CH}4$ for the Rh and Pd/MCMs was up to 1.8 % and 1.6 %, respectively, when $\lambda \geq 250$ nm. Φ_{CO} was lower than $\Phi_{CH}4$ owing to the existence of CO_2 generation as competition. Thermodynamically, the exothermic degree of POM (ΔH_{298K} = −35.9 kJ mol^{-1}) is much lower than that of the complete oxidation (ΔH_{298K} = −802.5 kJ mol^{-1}).[18] Therefore, a respective energy-intensive condition is usually required for POM. It is reasonable that the generation of CO needs a more stringent optical condition, which was $\lambda <$ 325 nm in the present study.

The energized electrons in metals are easy to relax and return to the ground state. Electron-electron and electron-phonon scattering occur during the relaxation, accompanied by the transformation of electron kinetic energy to the internal energy of the electron-phonon system, subsequently realizing the photothermal conversion. To confirm the hot-carrier-induced photothermal effect, we measured the surface temperatures of pristine MCM-41 and M/MCMs using an infrared (IR) sensor (Fig. S6a, ESI†). Under the dark conditions, the surface and operating temperatures of all the samples were approximately equal since the differences were less than 5 K. Under UV irradiation, the surface temperatures of commercial MCM-41 were no more than 20 K higher than the corresponding operating temperatures. However, photothermal effects were significant in M/MCMs, of which the increase in surface temperature was 200 K at a maximum, and there were good linear relations between the surface and operating temperatures. As shown in Fig. S6b and c (ESI†), the catalytic performance data of Rh and Pd/MCMs under the dark conditions and UV irradiation were reproduced by 3-dimensionally plotting the yield of CO (*z*-axis) as a function of operating temperature (*x*-axis) and surface temperature (*y*-axis). Even at the same surface temperature, syngas generation under UV irradiation was more efficient than that under the dark conditions. This result indicates that, although the photothermal effect is considered a critical factor in hot-carrier-driven photocatalysis, the elevation of surface temperature is insufficient to provide enough power to catalyze POM in the present case. A recent study suggested that the primary reason for high reaction rates would be the light-induced temperature gradients between the top-surface and bottom-surface of the catalyst bed.[19] However, in the present work, we excluded the contribution of temperature gradients to syngas evolution through a comparative study using another photothermal material (described in detail in Fig. S7, ESI†).

Therefore, we deduce that the hot carriers interacted directly with the surface-adsorbed gas molecules on metal nanoparticles, which can be described as hot carriers' nonthermal effect as follows. Hot electrons with high kinetic energy can migrate to the interface. O_2 can capture these hot electrons with its antibonding orbital, and be reduced to anionic oxygen species,[9] which is analogous to the conventional photocatalytic oxidation process. On the other hand, it has been identified that the hot holes (*i.e.*, electron-deficient $M^{\delta+}$ species) can facilitate the activation of CH_4 by despoiling its σ electrons.[12]

To evaluate the contribution of hot carriers' nonthermal effect to the photocatalytic POM, for all M/MCMs, we carried out the Arrhenius plots using the generation rate of CO (r_{CO}) as the dependent variable and the surface temperature (T_S) as the independent variable (Fig. S8, ESI). The apparent activation

energy for CO generation under the dark conditions ($E_{a,dark}$) was completely supplied by the external heating because it was a pure thermocatalytic case. The apparent activation energy under UV irradiation ($E_{a,UV}$) was together supplied by the external heating and photothermal effect. For Rh, Pd, and Ru/MCMs, $E_{a,UV} < E_{a,dark}$. The decrease in apparent activation energy after introducing UV light ($\Delta E_a = E_{a,dark} - E_{a,UV}$) can be attributed to the nonthermal effect of hot carriers. Therefore, the proportion $E_{a,UV}/E_{a,dark}$ and $\Delta E_a/E_{a,dark}$ can be defined as the contribution of thermal energy (including both the external heating and hot carriers' photothermal effect), and the contribution of hot carriers' nonthermal effect, respectively, as shown in Fig. 4b. Evidently, the hot carriers' nonthermal effect was the dominant factor in the photocatalytic POM over Rh and Pd/MCMs. However, in the case of Pt/MCM, $E_{a,UV} > E_{a,dark}$, which indicates that the generation of syngas was still driven by the thermal energy under illumination, and there was no significant contribution of hot carriers' nonthermal effect.

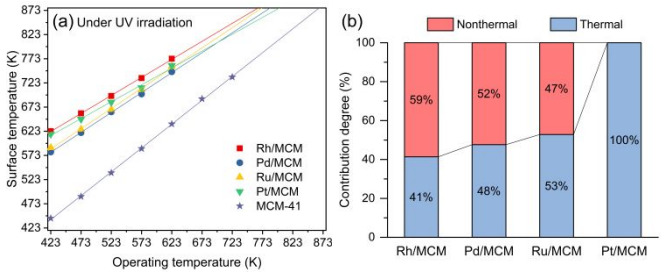

Fig. 4 (a) Surface temperatures of M/MCMs and commercial MCM-41 catalyst beds as functions of operating temperatures under UV irradiation. (b) Contribution degree of thermal energy (including external heating and photothermal effect) and hot carriers' nonthermal effect in the photocatalytic POM with respect to the apparent activation energy in a pure thermocatalytic case.

In conclusion, we demonstrated the enhancement of POM to produce syngas under UV irradiation by using noble metals (Rh, Pd, Ru, and Pt) incorporated in an MCM-41 molecular sieve. Rh/MCM exhibited superior photocatalytic performance at operating temperatures as low as 423 K with a stable output of syngas (CO selectivity of around 50%) in a flow system, and a quantum yield Φ_{CH_4} = 1.8 % under the condition of $\lambda \geq 250$ nm. The photocatalytic reaction is driven by photogenerated hot carriers from the *d*-to-*s* interband excitation in metal nanoparticles. The mechanism can be ascribed to the synergistic nonthermal effect of hot carriers: the direct activation of the O_2 and CH_4 adsorbed state by hot electrons and hot holes, and the photothermal effect resulting from the relaxation of hot carriers. The mechanism differs from the conventional semiconductor-based photocatalysis (Note 5, ESI†). We expect that this finding, as well as the concept of hot carriers, will enrich the systems of photocatalytic methane conversion and contribute to the progress of heterogeneous catalysis for optical energy conversion.

This work was financially supported by Japan Science and Technology Agency (JST) CREST (No. JPMJCR15P1) and Japan Society for the Promotion of Science (JSPS) Kakenhi (No. 18H02055). H. Jiang was sponsored by the China Scholarship Council (No. 201708050022). We appreciate the help of Ookayama Materials Analysis Division, Tokyo Institute of Technology, for TEM and ICP-MS tests. We would like to thank Editage (www.editage.jp) for English language editing.

Conflicts of interest

There are no conflicts to declare.

Notes and references

1 (a) B. Christian Enger, R. Lødeng and A. Holmen, *Appl. Catal. Gen.*, 2008, **346**, 1–27; (b) R. C. Baliban, J. A. Elia, V. Weekman and C. A. Floudas, *Comput. Chem. Eng.*, 2012, **47**, 29–56.
2 S. A. Al-Sayari, *Open Catal. J.*, 2013, **6**, 17–28.
3 (a) L. Yuliati and H. Yoshida, *Chem. Soc. Rev.*, 2008, **37**, 1592–1602; (b) A. Kudo and Y. Miseki, *Chem. Soc. Rev.*, 2009, **38**, 253–278; (c) T. Hisatomi, J. Kubota and K. Domen, *Chem. Soc. Rev.*, 2014, **43**, 7520–7535.
4 (a) K. Shimura, H. Kawai, T. Yoshida and H. Yoshida, *ACS Catal.*, 2012, **2**, 2126–2134; (b) S. Wibowo, A. Yamaguchi, S. Shoji, T. Fujita, H. Abe and M. Miyauchi, *Chem. Lett.*, 2018, **47**, 935–937; (c) S. Shoji, A. Yamaguchi, T. Yamamoto, S. Matsumura, T. Fujita, X. Peng, H. Abe and M. Miyauchi, in *IPS-22 Conference*, Hefei, 2018.
5 (a) Y.-H. Chiu, S. B. Naghadeh, S. A. Lindley, T.-H. Lai, M.-Y. Kuo, K.-D. Chang, J. Z. Zhang and Y.-J. Hsu, *Nano Energy*, 2019, **62**, 289–298; (b) K.-H. Chen, Y.-C. Pu, K.-D. Chang, Y.-F. Liang, C.-M. Liu, J.-W. Yeh, H.-C. Shih and Y.-J. Hsu, *J. Phys. Chem. C*, 2012, **116**, 19039–19045; (c) I. Pastoriza-Santos, A. Sánchez-Iglesias, B. Rodríguez-González and L. M. Liz-Marzán, *Small*, 2009, **5**, 440–443.
6 (a) C. Clavero, *Nat. Photonics*, 2014, **8**, 95–103; (b) S. Sarina, H.-Y. Zhu, Q. Xiao, E. Jaatinen, J. Jia, Y. Huang, Z. Zheng and H. Wu, *Angew. Chem. Int. Ed.*, 2014, **53**, 2935–2940; (c) U. Aslam, V. G. Rao, S. Chavez and S. Linic, *Nat. Catal.*, 2018, **1**, 656.
7 X. Zhang, X. Li, D. Zhang, N. Q. Su, W. Yang, H. O. Everitt and J. Liu, *Nat. Commun.*, 2017, **8**, 14542.
8 H. Robatjazi, H. Zhao, D. F. Swearer, N. J. Hogan, L. Zhou, A. Alabastri, M. J. McClain, P. Nordlander and N. J. Halas, *Nat. Commun.*, 2017, **8**, 27.
9 P. Christopher, H. Xin and S. Linic, *Nat. Chem.*, 2011, **3**, 467–472.
10 W. Zhou, D. Jiang, J. Xue and X. Li, *CrystEngComm*, 2019, **21**, 30–33.
11 L. Zhou, D. F. Swearer, C. Zhang, H. Robatjazi, H. Zhao, L. Henderson, L. Dong, P. Christopher, E. A. Carter, P. Nordlander and N. J. Halas, *Science*, 2018, **362**, 69–72.
12 H. Song, X. Meng, Z. Wang, Z. Wang, H. Chen, Y. Weng, F. Ichihara, M. Oshikiri, T. Kako and J. Ye, *ACS Catal.*, 2018, **8**, 7556–7565.
13 D. Takami, Y. Ito, S. Kawaharasaki, A. Yamamoto and H. Yoshida, *Sustain. Energy Fuels*, in press.
14 H. Huang, M. Mao, Q. Zhang, Y. Li, J. Bai, Y. Yang, M. Zeng and X. Zhao, *Adv. Eng. Mater.*, 2018, **8**, 1702472.
15 (a) A. T. Ashcroft, A. K. Cheetham, M. L. H. Green and P. D. F. Vernon, *Nature*, 1991, **352**, 225–226; (b) P. D. F. Vernon, M. L. H. Green, A. K. Cheetham and A. T. Ashcroft, *Catal. Today*, 1992, **13**, 417–426.
16 J. Alan Creighton and D. G. Eadon, *J. Chem. Soc. Faraday Trans.*, 1991, **87**, 3881–3891.
17 C.-T. Au, C.-F. Ng and M.-S. Liao, *J. Catal.*, 1999, **185**, 12–22.
18 D. R. Lide, Ed., *CRC Handbook of Chemistry and Physics, 85th Edition*, CRC Press, 2004.
19 X. Li, X. Zhang, H. O. Everitt and J. Liu, *Nano Lett.*, 2019, **19**, 1706–1711.